Influence of multilayer nanoarchitecture on phase transformations in the Ti-Cr-Zr system

Júlia Nascimento Pereira [a,*], Vincent Ott [b], Conrado Ramos Moreira Afonso [c], Artur Mariano de Sousa Malafaia [d], Michael Stüber [b], Christian Greiner [b], Haroldo Cavalcanti Pinto [a]

[a] Center for Research and Analysis of Engineering Materials (CEPAME), São Carlos School of Engineering (EESC), University of São Paulo (USP), Brazil
[b] Institute for Applied Materials (IAM), Karlsruhe Institute of Technology (KIT), Germany
[c] Federal University of São Carlos (UFSCar), Brazil
[d] Federal University of São João del Rei (UFSJ), Brazil

Keywords:
Nano multilayers
Nanocrystalline metals
Diffusion
Heat treatment
Ti-Cr-Zr

A B S T R A C T

Nanocrystalline thin films find extensive applications due to their high mechanical strength and wear resistance. However, the challenge is to prevent unwanted grain growth during operation, especially at high temperatures, due to the increased grain boundary volume, which elevates the system's overall energy. Addressing this issue necessitates identifying optimal heat treatment conditions and selecting appropriate chemistry to stabilize grain boundaries. This study investigates the grain growth and phase evolution within Ti-Cr-Zr magnetron sputtered nano multilayers with 5 and 10 nm individual layer thickness, subjected to vacuum heat treatment at 1100 °C for 5 and 10 min. Characterization involved X-ray Photoelectron Spectroscopy (XPS), X-Ray Diffraction (XRD), and Transmission Electron Microscopy (TEM). During deposition, evidence of diffusion was observed as the multilayers formed Cr_4TiZr, $TiCr_2$, and Cr_2Zr, phases. The Ti-Cr-Zr nanoscale system multilayers with 10 nm individual layer thickness also exhibited the emergence of $Ti_{0.3}Zr_{0.7}$ phase. During heat treatment grain growth occurred, after 10 min an average grain size of 173.7 nm and 119.1 nm was noted for the Ti-Cr-Zr nanoscale system multilayer with 5 nm and 10 nm individual layer thickness, respectively. The different growth rates are attributed to their distinct interfacial volumes, influencing the reaction velocity due to the variations in nanolayer thickness. No new phases were formed after heat treatment for the case of 10 nm individual layer thickness coating. However, 5 nm individual layer coatings showed the emergence of $Ti_{0.3}Zr_{0.7}$ phase, not present after deposition. In conclusion, this research achieved the desired nano grain stabilization of the Ti-Cr-Zr system nanoscale multilayers after heat treatment at 1100 °C for 10 min. This process led to the complete decomposition of the multilayer structure, resulting in the formation of grains smaller than 200 nm, marking a significant step toward the effective control of grain growth in nanocrystalline materials.

1. Introduction

Nanocrystalline metallic materials can exhibit high mechanical strength [1–3] and wear resistance [4,5], as well as, desirable chemical and physical properties such as superior resistance to corrosion [6] and irradiation [7]. Nanocrystalline thin films hold considerable attraction for a diverse range of applications, including electronic devices, optical coatings, wear-resistant surfaces, and decorative components. The literature continues to introduce innovative applications and novel devices in this field. These materials have attractive properties due to their high interface density and lattice imperfections. Nonetheless, the significant grain boundary volume increases the system's overall energy, consequently promoting grain growth [8]. Remarkable enlargement of grain size at temperatures considerably lower than those conventionally needed for material processing, such as powder consolidation or sheet-metal forming, has been documented [9,10]. Notably, certain investigations have even reported coarsening occurring at ambient room temperature [11–13]. To address this issue, modifications are important to establish structurally and energetically stable interfaces, effectively mitigating unwanted grain growth [14,15]. Thus, it is imperative to

* Corresponding author.
E-mail addresses: julianp@usp.br (J.N. Pereira), vincent.ott@kit.edu (V. Ott), conrado@ufscar.br (C.R.M. Afonso), arturmalafaia@ufsj.edu.br (A.M. de Sousa Malafaia), michael.stueber@kit.edu (M. Stüber), christian.greiner@kit.edu (C. Greiner), haroldo@sc.usp.br (H.C. Pinto).

introduce alterations to the grain boundaries within nanocrystalline thin metallic films. Appropriate selection of deposition techniques, thin film growth, thin film thickness and other characteristics are essential.

The initial step involves the production of materials with nanoscale grains. An effective strategy to achieve this goal entails the fabrication of coatings through magnetron sputtering. This technique not only yields the intended initial nanostructure morphology but also offers numerous advantages such as precise control over film thickness, uniformity, high purity and good adhesion to the substrate [16]. Following this, subjecting these films to a carefully tailored heat treatment can lead to grain boundary segregation, precipitation, and/or formation of new phases at the grain boundaries. These phenomena play a significant role in stabilizing the grain boundaries and hindering the undesirable progression of grain growth, thereby preserving the wanted properties of the nanostructures even at elevated temperatures [2,17–20]. By carefully selecting the appropriate materials and optimizing parameters for the heat treatment process, such as temperature and duration, the stability of the coatings can be assured. However, a challenge is to determinate those parameters and choose the chemistry that achieves this grain boundary stabilization.

The stability of grain sizes in binary nanocrystalline systems has been extensively investigated across a wide range of materials, such as Cu—Zr, Cu—Hf, Hf—Ti, W—Cr, Fe—Mn, Ta—Hf, among others [3,19,21–25]. However, the exploration of phase and microstructure formation in a ternary Ti-Cr-Zr thin film system with varying nano-layer thicknesses annealed after deposition remains unknown. These metals are notorious for their mechanical properties, corrosion and wear resistance [26–28]. Laves phases can be found in the binary sub-systems, such as Cr_2Ti, Cr_2Zr, which exhibit promising mechanical properties, as well as corrosion and oxidation resistance [29,30]. These phases, categorized as a significant class of topologically close-packed structures, have been extensively reported in metallic materials, including Ti-based alloys [31,32]. Consequently, Laves phases have found widespread utility in both structural and functional applications. For instance, they can enhance the mechanical properties of alloys [33,34], serve as hydrogen storage materials [35,36], function as corrosion [37] or wear-resistant coatings [38], and even exhibit magnetic properties [39]. These phases are characterized by their chemical formula, AB_2, with A and B representing the larger and smaller atoms, respectively. Furthermore, the ternary system shows the feature of mutual solid solubility under specific conditions, leading to the formation of diverse thin film microstructures after annealing, thus adding complexity and interest to the system. Furthermore, the diffusion and formation of intermetallic compounds hold the potential to enhance grain stability at the nanoscale [21,40]. Murdoch and Schuh [2] developed an approach for calculating the segregation enthalpy of binary systems and estimate if a dopant has potential to segregate to the grain boundary. In the case of the binary systems Ti—Cr, Zr—Cr and Ti—Zr, they present positive ΔH^{seg} indicating potential to solute segregation [2]. Consequently, it is anticipated that Ti-Cr-Zr system nanoscale multilayer systems will exhibit nano grain stabilization at high temperatures by the formation of precipitates. According, to Ti—Cr phase diagram, at 1100 °C, either a β-(Ti,Cr) solid solution or $TiCr_2$ intermetallic can form depending on the atomic percentage of each element [41]. Similarly, the Zr—Cr phase diagram indicates the potential for the formation of a β-(Zr,Cr) solid solution or $ZrCr_2$ intermetallic at 1100 °C [42]. In the Ti—Zr phase diagram, a β-(Zr, Ti) solid solution can be observed at 1100 °C [43]. Additionally, in the ternary Zr-Ti-Cr diagram, the phases body cubic center (BCC_A2), hexagonal close packed (HCP_A3) and Laves (C15) can be formed at 800 °C [44]. Zr and Cr serve as β-stabilizing elements in Ti—Zr alloys. Notably, even with a 5 % content of Cr, a stabilization of β phase is observed [45]. At 1100 °C, the expected phases include BCC_A2 $Ti_{0.3}Zr_{0.7}$ (with the possibility of some Cr presence), C14_Laves $TiCr_2$, and C15_Laves Cr_2Zr (with little or no Ti solubility), according to Thermo-Calc approach shown in Fig. 1. Varying the design of multilayers, such as the thickness of individual layers, corresponds to different compositional points on the phases diagram. Depending on the thermodynamics and kinetics of mass and heat transport within nanoscale metal systems, the evolution of various phases in these regions of the diagrams may or may not occur [46].

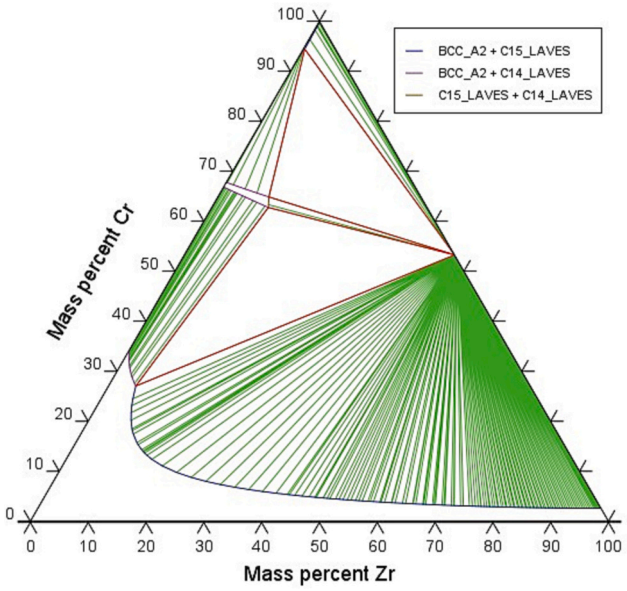

Fig. 1. Ternary phase diagram of Ti-Cr-Zr system at 1100 °C.

Thus, the main objective of this research is to analyze the effect of the heat treatment at 1100 °C for 5 and 10 min within the Ti-Cr-Zr nano metallic multilayers with 5 and 10 nm layer thickness. Given that the grain size in the as-deposited state is influenced by the thickness of individual layers, a few-nanometer layer thicknesses were chosen. Furthermore, considering that nanoscale layer thicknesses can influence the diffusion pathways necessary for transformations, this parameter was systematically varied. The total interfacial area is indirectly controlled through the selection of layer thicknesses and the number of layers. When maintaining the total coating thickness at 4.5 μm, Ti-Cr-Zr nanoscale system multilayers with 10 nm individual layer thickness feature twice the interfacial area and nano-layers in comparison to the system with 5 nm individual layers. This control over multilayer structure provides the means to tailor reaction speed [47]. In order to facilitate the possibility of intermetallic formation during high-temperature heat treatment, a temperature of 1100 °C was chosen This temperature aligns with the known reaction temperature for the formation of intermetallics between the binary systems Ti—Cr and Cr—Zr, as indicated in the phases diagrams [41,42]. This study primarily focuses on understanding the phases transformations, decomposition of the multilayers, and grain growth during the initial minutes of the heat treatment. Subsequent work will observe the behavior of the coatings as heat treatment duration increases. The objective is to note weather, after 10 min of heat treatment, the grains maintain their nanoscale dimensions and if any precipitates or new phases are formed. These finds are expected to yield substantial enhancements in the material's mechanical and tribological properties, which will be subject to future investigation. These discoveries will offer valuable insights into the interplay of composition, deposition, layer thickness and heat treatment parameters that govern the microstructure, properties, and behavior of nano metallic multilayers.

2. Experimental details

2.1. Coating deposition

Nanostructured multilayers consisting of pure Ti, Zr, and Cr layers

were fabricated using DC magnetron sputtering on polished, c-oriented sapphire substrates measuring 10x10x1 mm. Prior to the deposition process, these substrates were cleaned in an ultrasonic bath with acetone for 15 min. The Ti, Zr, and Cr sputtering targets were cleaned by pre-sputtering for 5 min at the same power to eliminate potential surface contaminants. A shutter mechanism ensured that the substrates remained uncoated during this preparatory phase. These depositions were conducted under a pressure of 0.4 Pa, with the residual gas pressure being approximately 5×10^{-6} mbar before the introduction of the high-purity Ar 6.0 (99.9999 % purity) working gas. The applied power to the targets was set at 80 W (radio frequency - RF) for Zr, 40 W (direct current - DC) for Ti and 60 W (DC) for Cr. The cylindrical targets, with a diameter of 75 mm, were symmetrically arranged at 90° in the deposition chamber and affixed to a water-cooled Cu holder. The purity of the respective targets was Zr 3 N5 (99.95 %), Ti 4 N5 (99.995 %), Cr 3 N5 (99.95 %). The multilayer architecture was achieved in the top-down sputtering process, employing sequential deposition in a stop-and-go mode. This was facilitated by a rotating substrate holder positioned at a vertical distance of 50 mm from the targets. By varying the dwell time beneath each target, distinct layer thicknesses were achieved in correspondence with the applied powers. During the sequential deposition of the multilayers structure, a shutter mechanism was utilized, without the application of a substrate bias (i.e., the substrates were grounded) and without substrate heating. The purpose of employing the shutter mechanism was to guarantee the deposition of one metal from a pure target at a time. Consequently, while depositing a pure titanium layer, the chrome and zirconium targets were shielded to prevent their deposition. Similarly, when depositing a layer of pure chrome, the titanium and zirconium targets were protected, and this process was repeated for each subsequent layer. Therefore, the multilayers consisted of alternating pure metals layers, with the final top layer consisting of pure Cr. The total thickness of the coatings was 4.5 μm. The study focused on investigating the Ti-Cr-Zr stacking sequence along with two different layer periodicities of 5 and 10 nm.

2.2. Heat treatment

The ternary Ti-Cr-Zr system nanoscale multilayers were annealed at 1100 °C for 5 and 10 min, following the recommendations of [48]. These annealing processes were conducted under vacuum conditions with a pressure approximately equal to 10^{-3} mbar. It was done inside a quartz vertical tube furnace. The used furnace is equipped with vertical movement capability, allowing control over the sample's exposure to heat. When the furnace was in the lowered position, the samples remained outside of it. Conversely, as the furnace ascended, the samples were inserted into the furnace, where they were subjected to the desired temperature conditions. The heat treatment process can be divided into four stages. In stage 1, the furnace was heated while the samples remained outside at room temperature and vacuum pressure. The heating hate was 20 °C/min, taking approximately 54 min to reach 1100 °C, starting from room temperature. In stage 2, the furnace reached the target temperature and moved upward, allowing the samples to be placed inside. Both the samples and the tube furnace were at room temperature, causing the furnace temperature to drop quickly to around 850 °C. However, within just 15 min, the furnace rapidly regained 97 % of the target temperature. In stage 3, the actual heat treatment duration started for 5 or 10 min. Finally, in stage 4, the tube with the samples was taken from the furnace and cooled with blown air at room temperature without breaking the vacuum. The cooling rate was high, and the samples took about 7 min to reach approximately 65 °C. This deliberate choice in cooling speed was made to observe the initial phase's transformation, as a slower cooling process would allow further transformations to occur. Thermodynamic equilibrium calculations were carried out using the program Thermo-Calc and the TCFe13 database [49] which contains a proper description of the binary and ternary diagrams of the elements Ti, Zr, and Cr.

2.3. Coating characterization

X-ray diffraction (XRD) was performed to identify the phases in the as-deposited and heat-treated coatings. XRD patterns were collected using a Panalytical MRD-XL X-ray diffractometer in Bragg-Brentano mode, utilizing Mo-Kα radiation (0.7093 Å). X-ray photoelectron spectroscopy (XPS) analysis was conducted to investigate the chemical depth profiles of the initial conditions of the as-deposited Ti-Cr-Zr stacking sequence multilayers. A K-alpha X-ray photoelectron spectrometer system was used with a micro-focus tube with Al-Kα radiation, an etching time of 10 s/step using an Ar cannon and a 2000 eV beam energy were used to determine the chemical depth profiles. The etch rate for the Ta_2O_5 using Ar ions was utilized in the calculations [50]. Transmission electron microscopy (TEM) analysis of as-deposited and annealed samples was conducted to observe the multilayer structure, grain size, grain boundary distribution, grain orientations and the distribution of the phases. The cross-section samples were prepared by ion beam milling. TEM images were acquired using an FEI TECNAI G2 F20 HRTEM microscope. Dark-Field (DF-TEM), High-Angle Annular Dark-Field (HAADF), High-Resolution (HR-TEM) and Selected Area Electron Diffraction (SAED) images, as well as Energy dispersive spectroscopy (EDS) line analysis, were performed at 200 kV. Furthermore, Scanning Transmission Microscopy (STEM) images and EDS maps were done in focused ion beam (FIB) prepared lamellas of the 10-min heat treated coatings using a Thermo Fisher FEI Titan Cubed Themis TEM operating at 300 kV at the LNNano. The cross-section lamellae were prepared on a Thermo Fisher Dual Beam Scios 2 microscope also at LNNano. Grain sizes were determined through the analysis of DF-TEM and STEM images using ImageJ software.

3. Results

3.1. As-deposited coatings

Ti-Cr-Zr system nanoscale multilayers with 5 and 10 nm individual layer thickness were fabricated by magnetron sputtering. The depth-resolved XPS results in Fig. 2 provide insights into the Ti-Cr-Zr as-deposited coatings. When examining the multilayers with 5 nm individual layer thickness, Fig. 2a, a mixed composition is observed, indicating some level of intermixing. However, as the nanolayer thickness increases, a clear modulation in chemical composition becomes more pronounced, in the case of a 10 nm periodicity, Fig. 2b. This variation suggests the presence of distinct layers richer in chromium, others in zirconium, and others in titanium.

Fig. 5 shows the XRD results for the as-deposited Ti-Cr-Zr system nanoscale multilayers. The gray and green lines represent as-deposited coatings with individual layer thickness of 5 and 10 nm, respectively. These diffractograms clearly exhibit multiple reflexes, indicative of the polycrystalline and nanocrystalline nature of the materials. Most of the reflexes are relatively broad and do not readily correspond to individual phases. However, in the case of the 5 nm as-deposited coating, the diffraction peak with an approximate center around 16° extends to positions associated with both the (100) crystallographic orientation of pure Ti (ICSD #253841) and (022) crystallographic orientation of pure Zr (ICSD #253515). Nevertheless, this peak is so broad that it also encompasses positions linked to other phases. Consequently, it is challenging to definitively assign this broad signal to a single pure metal phase. A similar situation is observed for the 10 nm coating. The diffractions of the as-deposited coatings suggest the presence of pure metal and intermetallic phases such as Cr_2Zr (ICSD #52072) and $Cr_4(TiZr)$ (ICSD #626922), though further confirmation is necessary through other characterization techniques. Cr_2Zr was anticipated and known as Laves phase, while $Cr_4(TiZr)$ is a relatively unknow phase in the literature being mentioned in 1980 as a C14 structure phase [51] and as a Bergman cluster in 1997 [52].

HAADF-TEM imaging of the Ti-Cr-Zr system nanoscale multilayers

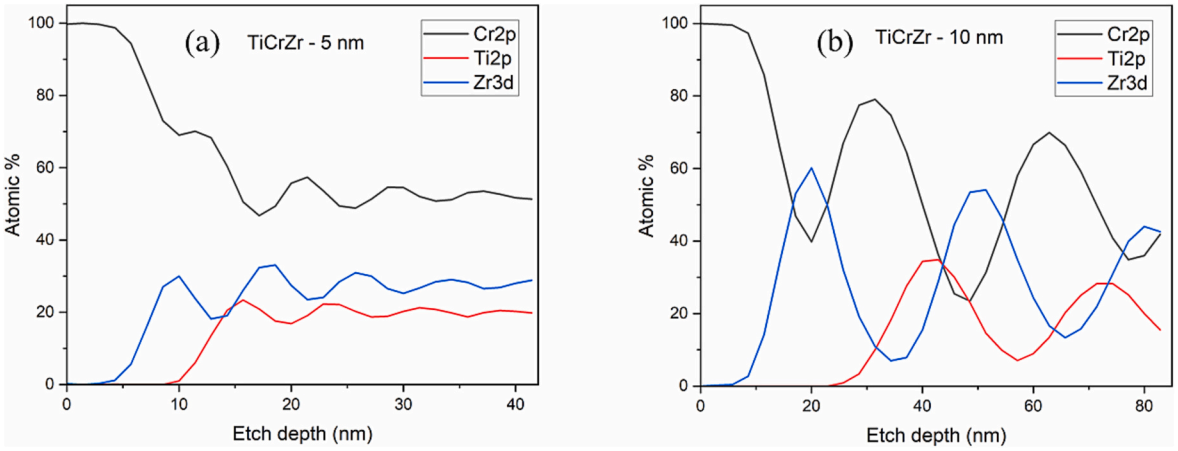

Fig. 2. XPS depth profile of Cr2p, Ti2p, and Zr3d of Ti-Cr-Zr system nanoscale multilayers with (a) 5 and (b) 10 nm layer thickness.

with 5 nm of layer thickness (depicted in Fig. 3a) shows a discernible multilayer structure comprising three distinct layers. Among these, one layer appears darker, while the other two exhibit a subtly varied gray-scale tone. The layers exhibited a thickness of approximately 4.3 nm. An EDS line scan, illustrated in Fig. 3b, shows the distribution of Cr, Zr, and Ti across the deposited layers. The periodicity of 5 nm is maintained even with the diffusion and mixture of the elements during deposition. Notably enriched layers featuring higher concentrations of Ti, Cr, and Zr manifest at 5 nm intervals. Quantitative analysis reveals the composition of the Ti-enriched layer to be approximately 76.0 at.% of Zr, 15.4 at.% of Ti, and 8.6 at.% of Cr. Similarly, the Cr-enriched layer shows an approximate composition of 78.5 at.% of Zr, 18.7 at.% of Cr, and 2.8 at. % of Ti. The Zr-enriched layer demonstrates a composition of approximately 94.4 at.% of Zr and 5.6 at.% of Cr. In Fig. 3c, the SAED image can be observed. It reveals the presence of pure Ti and several intermetallic compounds, including Cr_4TiZr, $TiCr_2$, and Cr_2Zr. Notably, superimposed rings are noticeable in the Cr_4TiZr (012) and Cr_2Zr (311) diffraction patterns. The Cr_2Zr (040), $TiCr_2$ (027) and Cr_4TiZr (214) rings appear broader, suggesting a certain degree of amorphism.

In Fig. 4 (a), the HAADF-TEM image of the 10 nm individual layer thick multilayers is shown. It also reveals the presence of three distinct layers: one exhibiting a darker shade, while the other two shows shades of gray. These layers measured approximately 7.6 nm in thickness. Additionally, the SAED analysis identifies the presence of pure Zr, as well as intermetallic phases including Cr_2Zr, Cr_4TiZr, $Ti_{0.3}Zr_{0.7}$, with the substrate Al_2O_3 also being detected. Remarkably, in the diffraction patterns, the presence of superimposed rings can be observed in the Al_2O_3 (221) and Cr_4TiZr (013) reflections. The $TiCr_2$ (019) ring appears broader, indicating a certain level of amorphous structure.

3.2. *Heat-treated coatings*

A comparison of the x-ray diffractograms obtained from the as-deposited coatings and after heat treatment at 1100 °C for 5 and 10 min is presented in Fig. 5. After heat treatment, a noticeable change in the XRD patterns of both coatings is observed. The intensities of the diffraction's peaks associated more favorably with the pure metals in the coatings decrease after heat treatment is observed, accompanied by an increase in the intensities of diffraction peaks corresponding to the intermetallic phases Cr_2Zr and Cr_4TiZr. A decrease in the peaks broadening is observed after heat treatment. This can be due to grain growth and stress annihilation. In addition, it can be observed a noticeable difference in the XRD patterns when comparing the as-deposited and the heat-treated for 5 min coatings with those subjected to 10 min of heat treatment. The former two (as-deposited and after 5 min of heat treatment) exhibited more intense peaks corresponding to Cr_4TiZr (041) and Cr_2Zr (662). However, after a 10-min heat treatment, these peaks decrease in intensity, while the peaks associated to Cr_4TiZr (112) and Cr_2Zr (311) become more intense. This transition can be attributed to a change in orientation of these phases. Initially, during deposition and in the beginning of the heat-treatment (up to 5 min), the nucleation of new grains with epitaxial relationships with adjacent grains presenting the initial orientation may have occurred. However, between 5 and 10 min of heat treatment, as the grain growth process occurred, competition among different grain orientations happened, resulting in another orientation that minimized grain boundary energy. The initial grain orientation can also be influenced by the substrate orientation. Grains in the deposited coating have the capacity to nucleate and grow with the same crystallographic orientation as the substrate, a phenomenon called

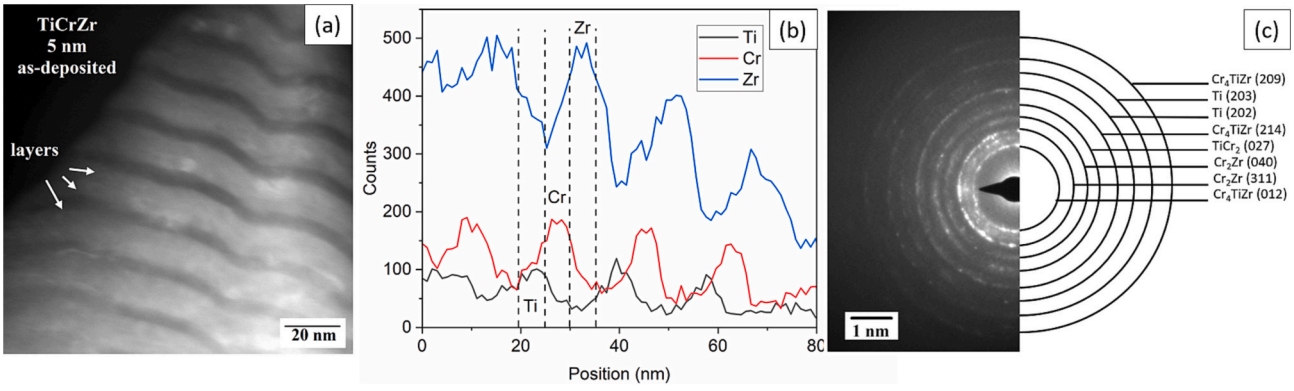

Fig. 3. (a) Cross-sectional HAADF-TEM image, (b) EDS line scan and (c) SAED image and scheme of identification of phases of as-deposited Ti-Cr-Zr with 5 nm layer thickness.

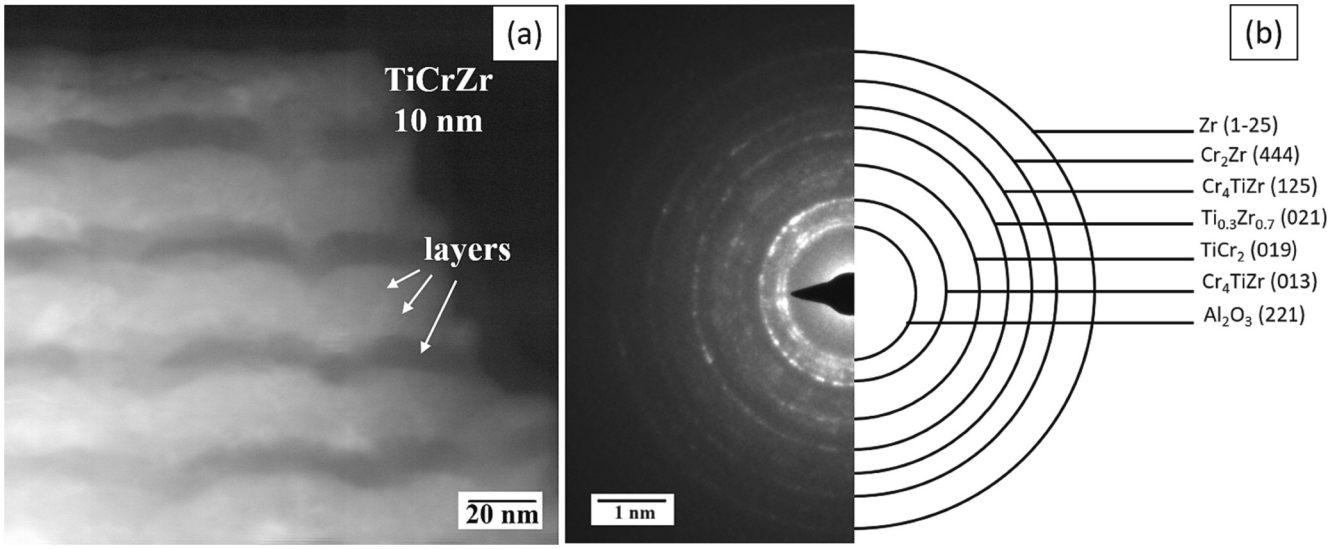

Fig. 4. (a) Cross-sectional HAADF-TEM image and (b) SAED image and scheme of identification of phases of as-deposited Ti-Cr-Zr with 10 nm layer thickness.

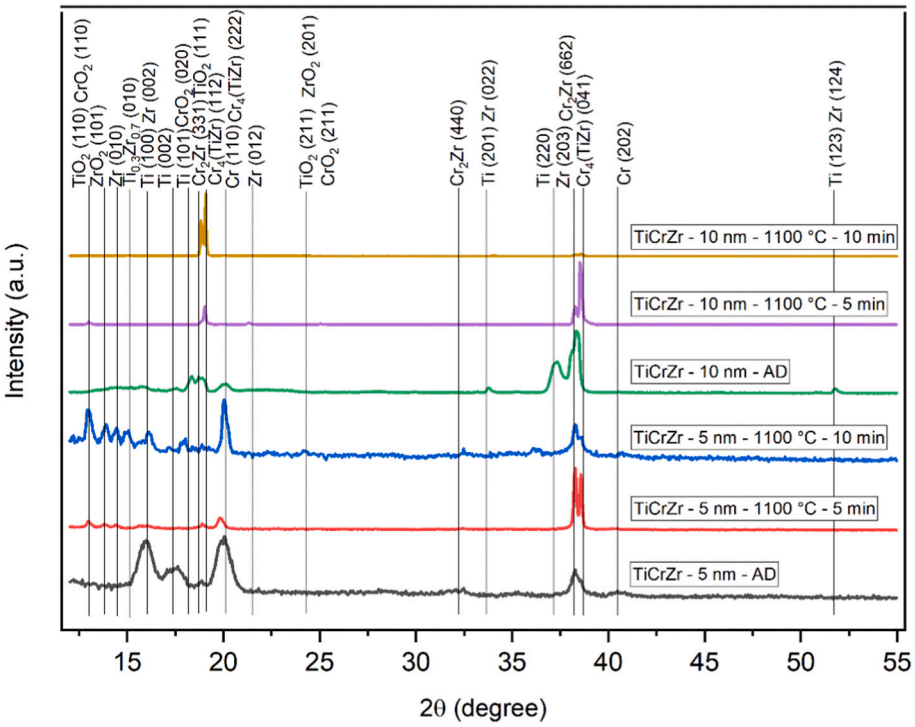

Fig. 5. Diffractograms obtained from Ti-Cr-Zr system nanoscale multilayers with 5 and 10 nm layer thickness as-deposited and after heat treatment at 1100 °C for 5 and 10 min.

epitaxial growth [53]. This interaction of nucleation, epitaxy, and grain growth dynamics contributes to the observed changes in the XRD patterns. Notably, despite the vacuum conditions during the heat treatment, oxidation occurred, as evidenced by the detection of TiO_2 (ICSD # 115504), CrO_2 (ICSD # 115492), and ZrO_2 (ICSD # 47794) oxides. This oxidation is notably more pronounced in the case of the 5 nm coatings.

Fig. 6 presents cross-sectional DF-TEM and HR-TEM images of the 5 nm individual layer thick Ti-Cr-Zr system nanoscale multilayers after a heat treatment at 1100 °C for 5 min. In Fig. 6a, the DF-TEM image reveals that the grains retained their nanoscale dimensions, with an approximate size of 5.0 nm, even after this high-temperature treatment. HR-TEM images in Fig. 6b-c show the microstructure, highlighting the presence of the intermetallic phase Cr_4TiZr and the solid solution phase $Ti_{0.3}Zr_{0.7}$ in the region shown, and areas where the material maintains its pure metal state (notably Zr in the region shown).

The results of the TEM characterization of the Ti-Cr-Zr system nanoscale multilayers with 5 nm thickness after an extended heat treatment at 1100 °C for 10 min are presented in Fig. 7. The STEM image in Fig. 7a reveals evident grain growth, with grains now measuring an average of 173.7 nm in size. The presence of several grains exhibiting deformation and elongation can be observed. Additionally, twin defects can be visualized within some of these grains. In the EDS map, it is evident that the elongated grains with twin defects exhibit a high Zr content (Fig. 7f). Nano-sized precipitates are distributed along grain boundaries and can also be found within the grains, with an average size of 19.4 nm. Grains rich in Cr presented an equiaxed shape, and there are

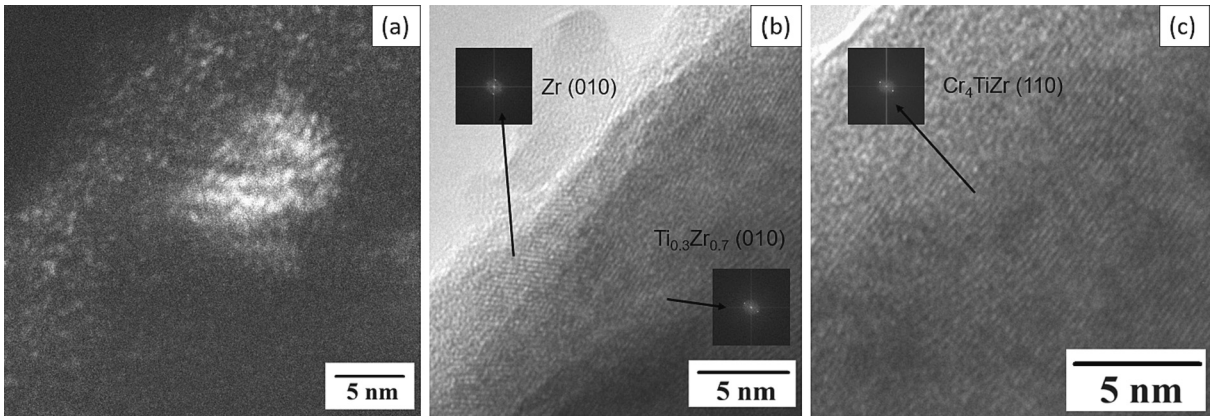

Fig. 6. Cross-sectional analysis of Ti-Cr-Zr system nanoscale multilayers with 5 nm layer thickness after heat treatment at 1100 °C for 5 min: (a) DF-TEM, (b) HR-TEM and (c) HR-TEM image of another region.

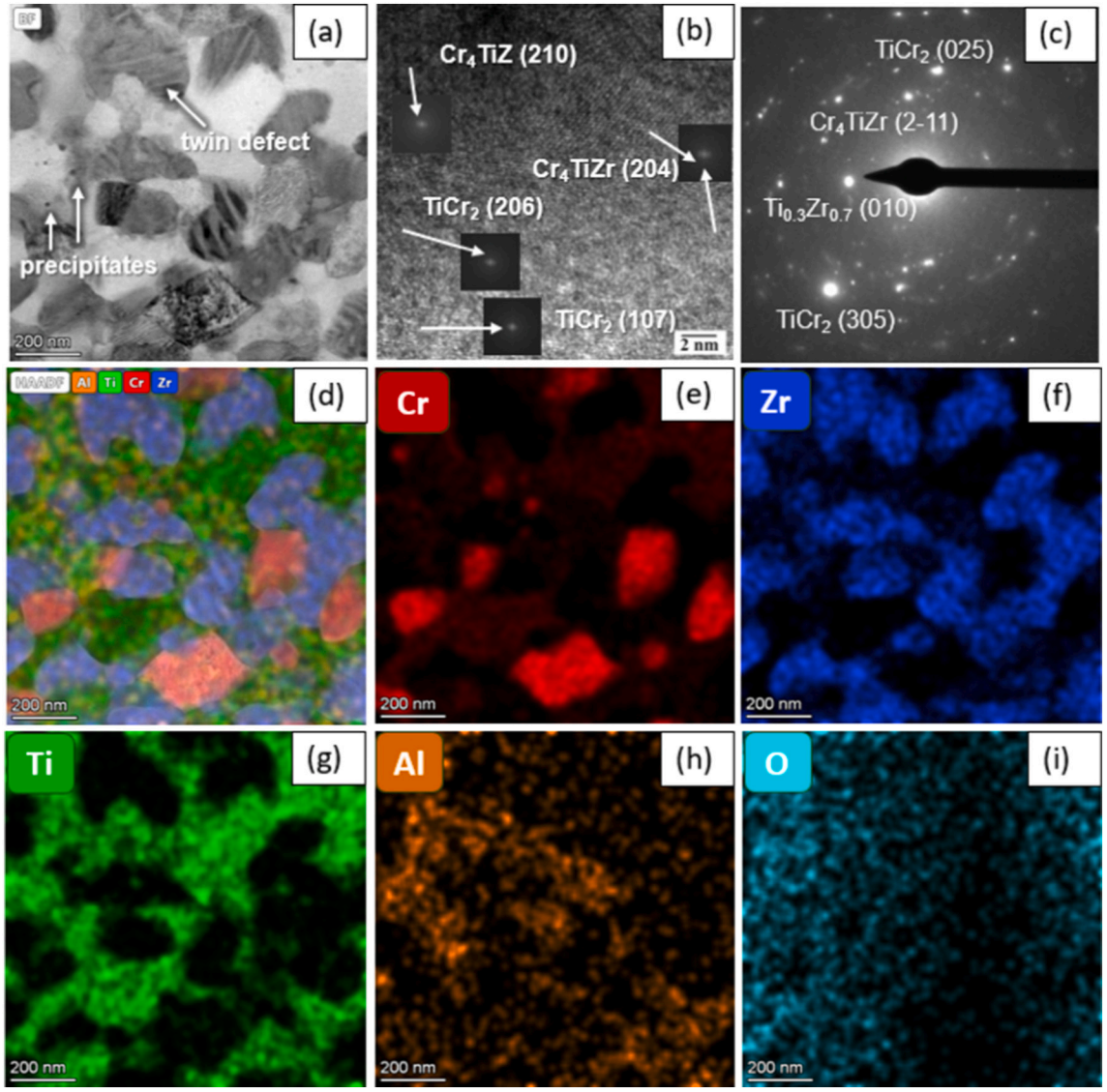

Fig. 7. Cross-sectional analysis of Ti-Cr-Zr system nanoscale multilayers with 5 nm layer thickness after heat treatment at 1100 °C for 10 min: (a) BF-STEM, (b) HR-TEM, (c) SAED image, and EDS maps for (d) Al, Ti, Cr and Zr, (e) Cr, (f) Zr, (g) Ti, (h) Al, and (i) O.

Cr-rich precipitates in the grain boundaries as well (Fig. 7e). Some oxygen contamination from the substrate or from the atmosphere during heat treatment is detected within the coating (Fig. 7i). Aluminum contamination from the substrate is also present, as it is shown in Fig. 7h. Further analysis using HR-TEM enabled the identification of grains consisting of Cr_4TiZr and Ti_2Cr in the region shown in Fig. 7b. Additionally, the SAED analysis not only detected the presence of the intermetallic compounds Cr_4TiZr and Ti_2Cr but also the co-existence of a $Ti_{0.3}Zr_{0.7}$ phase, Fig. 7c.

Fig. 8 shows the results of the TEM analysis of the Ti-Cr-Zr system nanoscale multilayers with 10 nm layer thickness subjected to heat treatment at 1100 °C for 5 min. The DF-TEM image, as shown in Fig. 8a, reveals the formation of distinct nanoscale grains with an approximate size of 7.6 nm. Furthermore, HR-TEM analysis depicted in Fig. 8b identifies the presence of the intermetallic compound Cr_4TiZr in the region shown, with varying orientations. Additionally, the existence of $TiCr_2$, $Ti_{0.3}Cr_{0.7}$, and Cr_2Zr phases is evident. In another region of the same sample, some grains retained their pure metal states (Ti and Zr), coexisting with the presence of the intermetallic compound Cr_4TiZr, as shown in Fig. 8c.

The results of the TEM analysis of the Ti-Cr-Zr system nanoscale multilayers with 10 nm thickness that underwent the heat treatment at 1100 °C for 10 min are shown in Fig. 9. The STEM image shows grains with an average size of 119.1 nm, as seen in Fig. 9a. Similar to the Ti-Cr-Zr system nanoscale multilayers with a 5 nm thickness, twin defects are also evident in some of these grains exhibiting a Zr-rich composition (Fig. 9f). Notably, the precipitates in this case show more pronounced growth, presenting an average size of 111.2 nm and a Cr-rich composition (Fig. 9e). This coating also exhibits Al and O contamination (Fig. 9h-i). Detailed examination through HR-TEM and SAED images, as seen in Fig. 9 b-c, reveals the presence of intermetallic compounds, such as Cr_4TiZr, and Cr_2Zr and the solid solution phase $Ti_{0.3}Zr_{0.7}$.

4. Discussion

4.1. As-deposited coatings

The XPS findings, shown in Fig. 2, indicate that nanoscale multilayers in the system Ti-Cr-Zr with thinner nanolayers (here intentionally 5 nm individual layer thickness) exhibit higher diffusion during the deposition process compared to those multilayers with thicker nanolayers (here intentionally 10 nm individual layer thickness). It is obvious that with increasing nanolayer thickness a clear modulation in chemical composition becomes more pronounced. Furthermore, this observation highlights the remarkable precision and high quality of the magnetron sputtering deposition technique in creating nano-layers that closely approach the intended thickness, also confirmed by the EDS line analysis, Fig. 3b. Although some diffusion occurred during deposition, as can be seen by XPS, TEM and XRD results, Figs. 2–5, the multilayer structure was achieved with three distinct layers shown in HAADF-TEM images in Figs. 3a and 4a. The darker layer corresponds to the Zr-enriched layer as Zr is a heavier element compared to Cr and Ti. The other two layers with similar tones of gray color correspond to the Ti and Cr-enriched layers as they have similar Zr content. It can be noted that these layers have an average thickness of 4.25 nm and 7.6 nm for the 5 nm and 10 nm thick multilayers, respectively. These dimensions are slightly smaller than the expected 5 and 10 nm, attributable to layer diffusion during the deposition process, as evidenced by the XPS and EDS analysis shown in Figs. 2 and 3b. Another potential factor contributing to this deviation could be attributed to imperfect sample preparation. When images are not captured in a strictly parallel orientation with respect to the coatings, the actual thickness values might deviate from those observed in the images.

Although enriched layers can be noticed, a mixed composition is indicated, with each layer containing Ti, Cr, and Zr. The detection of intermetallic compounds further affirms the intermixing and phase formation of the deposited pure metals. The reason why the as-deposited samples do not simply consist of distinct, stacked layers of Ti, Cr and Zr lies in the energetic nature of the incoming particles responsible for film formation, which consist of metal atoms of specific weights. Regarding the electrical potential of the individual targets, i.e., the target voltage, these metal atoms possess a defined energy as they impact on the growing surface, thereby facilitating adatom mobility and localized diffusion. Additionally, even though the substrates are grounded, i.e., substrate voltage is zero Volts, they still acquire a specific, small potential relative to the plasma. This potential is induced by electron bombardment, which heats the substrate slightly and further enhances atom mobility. Consequently, self-diffusion and the diffusion of Ti in Cr, Ti in Zr and similar interactions need to be considered within the system. In industrial PVD coatings, the interface width has been reported to exceed 1 nm [54]. This dimension represents a significant fraction of the volume within the 5 and 10 nm individual layer thickness of the multilayer system. Therefore, it is reasonable to anticipate that the interface would provide conditions for easier diffusion pathways.

Vacuum deposition technique methods establish precise heterostructures, characterized by customized interfacial areas and minimal void volumes. The total interfacial area is indirectly influenced by factors such as the selection of layer thicknesses, the number of layers included, and the inherent material properties. For instance, the crystalline structures of the materials, where Ti and Zr exhibit hexagonal characteristics, while Cr has cubic structure, play a crucial role in shaping the interfacial properties. This compatibility between these material structures further impacts the characteristics of the interface. Moreover, vacuum-based deposition methods offer an environment of

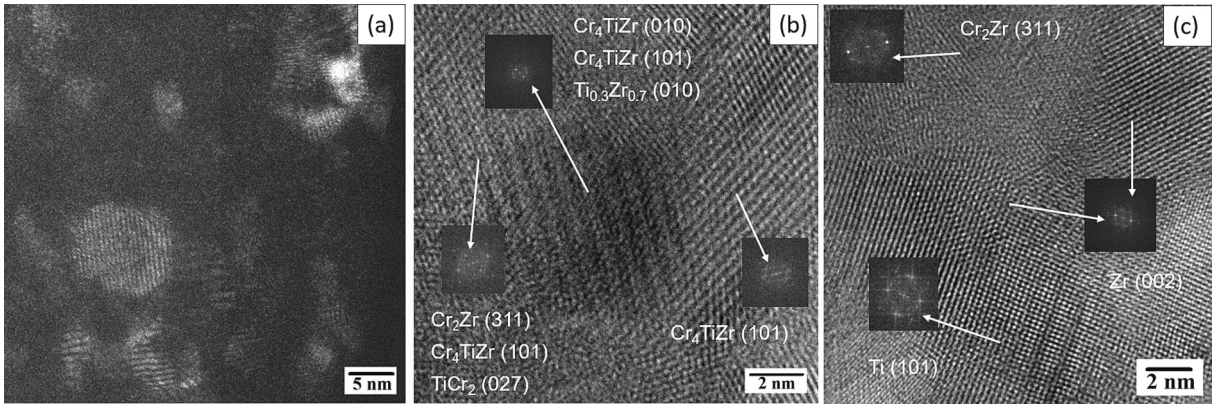

Fig. 8. Cross-sectional analysis of Ti-Cr-Zr system nanoscale multilayers with 10 nm layer thickness after heat treatment at 1100 °C for 5 min: (a)DF-TEM, (b) HR-TEM and (c) HR-TEM image of another region.

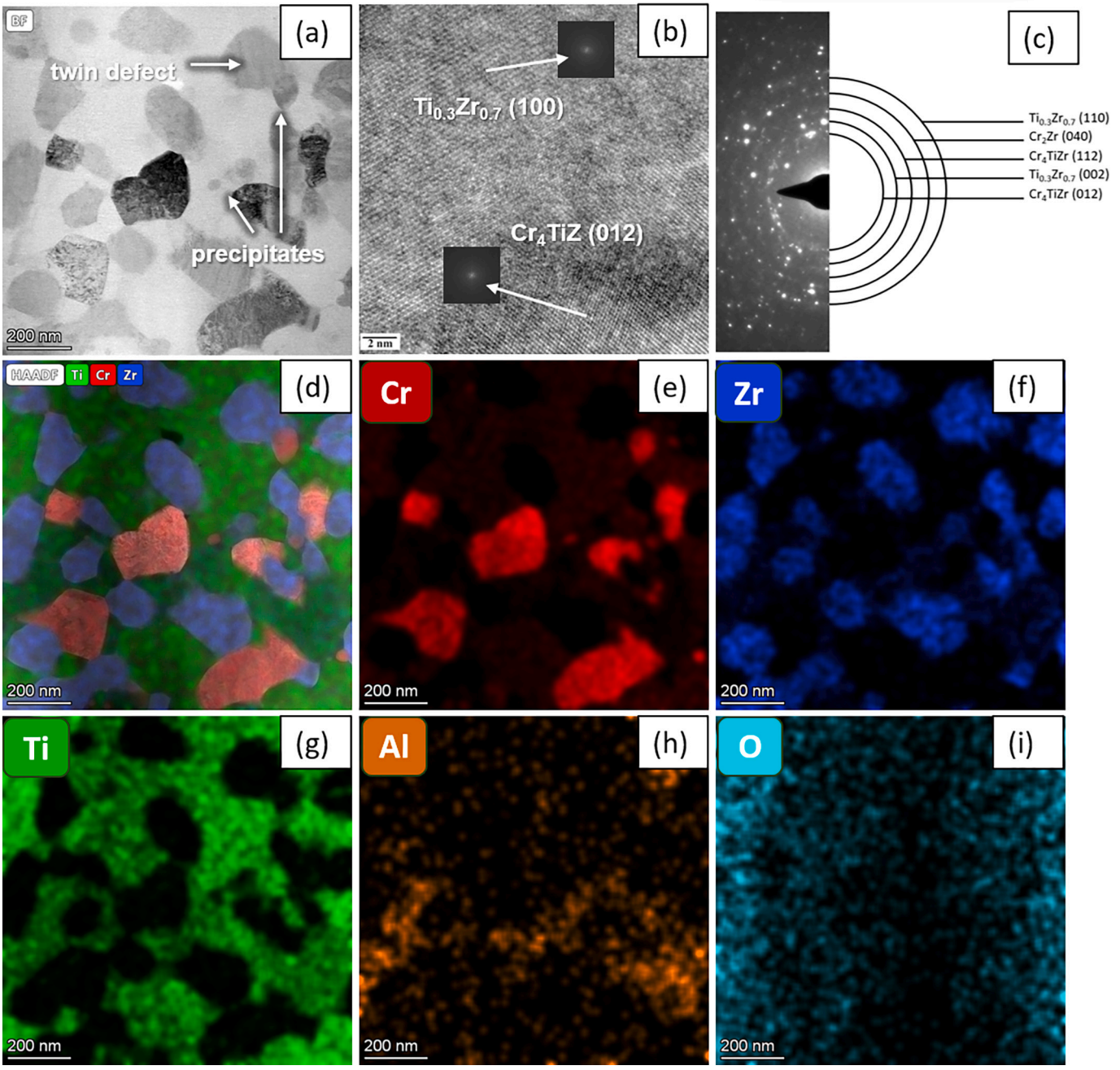

Fig. 9. Cross-sectional analysis of Ti-Cr-Zr system nanoscale multilayers with 10 nm layer thickness after heat treatment at 1100 °C for 10 min: (a) STEM, (b) HR-TEM, (c) SAED image, and EDS maps for (d) Al, Ti, Cr and Zr, (e) Cr, (f) Zr, (g) Ti, (h) Al, and (i) O.

utmost purity for thin film growth and open access to nanoscale dimensions. The ability to control multilayer composition and structure enables to manage for example reaction velocity in reactive multilayers [19,47,55,56]. Multilayers can undergo self-sustained exothermic reactions at high temperatures or when appropriately activated. These reactions are characterized by the propagation of a reaction wave front that advances through the energetic multilayer. In such vapor deposited multilayers, the relatively high reaction rates can be attributed to the combined influence of thin layers and favorable reaction kinetics. The underlying factors contributing to this phenomenon include a substantial interfacial area per unit volume, achieved using thin reactant layers, as well as high purity and minimal void volume. In practical terms, the velocity of the reaction wave front within a specific reactive multilayer system can be tailored by adjusting the thickness of the individual bilayers. Designs featuring thinner multilayers and a large interface area per unit volume tend to achieve higher propagation speeds due to reduced effective diffusion lengths [47].

While no exothermic reactions were observed in the Ti-Cr-Zr nanoscale system multilayers, it is important to note that mass and heat transport may have occurred during deposition. A relevant example can be found in Ru—Al multilayers, which constitute a rather exothermic system. In this case, a low heating rate has been reported to be effective in suppressing exothermic reactions, at least in very small local areas. This approach offers control over phase formation, ultimately leading to the desired result, such as the formation of the B2 phase RuAl [46]. The Ti-Cr-Zr system is notably complex. However, given the emergence of new phases during deposition process, it is possible that there is reactivity of the multilayers, especially in local areas.

The two as-deposited coatings exhibit remarkable similarity, both containing pure metal phases, along with the intermetallic phases Cr_2Zr,

$TiCr_2$ and Cr_4TiZr. The 10 nm structured coating also contains the $Ti_{0.3}Zr_{0.7}$ phase. The presence of Cr_2Zr, $TiCr_2$ and $Ti_{0.3}Zr_{0.7}$ was expected, as these phases were already indicated in the Cr—Zr [42], Ti—Cr [41], Ti—Zr [43] and Zr-Ti-Cr phase diagrams, Fig. 1. Of particular significance are the Laves phases, Cr_2Zr, $TiCr_2$, as they hold great promise due to their favorable mechanical properties, corrosion resistance, and oxidation resistance [29,30].

4.2. Heat-treated coatings

XRD diffractograms shown in Fig. 5 indicate that after heat treatment at 1100 °C diffusion processes occurred since the initial minutes. The multilayers exhibited diffusion of the elements, resulting in an increased presence of the intermetallics, Cr_2Zr and Cr_4TiZr, and a decrease in the proportion of pure metallic elements. Utilizing nano metallic multilayers enables precise modulation of phase formation within binary systems during annealing processes [21]. This effect is particularly notable due to the enlarged interface density inherent to nanoscale multilayers, which accelerates the velocity of phase transformations. As a result, thermal reactions can be elucidated at lower temperatures and/or shorter time, offering a significant advantage. Phase formation is dependent on the nanoscale multilayer architecture. An example of this is the formation of the intermetallic RuAl phase from the elemental layers, achieved at 600 °C through a meticulously designed multilayer structure [46]. Another example is the formation of an amorphous W_3Cr intermetallic compound at a notably reduced temperature of 1000 °C [21]. The distinctive multilayered arrangement exerts a significant influence on the kinetics of phase separation, effectively guiding the process toward the generation of solid solutions. Furthermore, a study has shown a notable grain growth behavior within nanocrystalline thin copper films compared to their conventional coarse-grained materials. Within this context, the mobility of grain boundaries in nanocrystalline copper film surpasses that of microcrystalline one, accompanied by a significant reduction in the activation energy required for grain growth. Consequently, this material demonstrated the ability to undergo grain growth even at low temperatures [9]. These findings provide evidence of structural transformations and the formation of intermetallics during the initial minutes of the heat treatment process.

The TEM images, Figs. 6–9, show the grain growth of the Ti—Cr—Zr system nanoscale multilayers. In the case of Ti—Cr—Zr with 5 nm layer thickness, the grains exhibited an average size of 5.0 nm after undergoing a 5-min heat treatment at 1100 °C, Fig. 6a. However, after a 10-min treatment, the grains grew significantly, reaching an average grain size of 173.7 nm, Fig. 8a. Although the initial layers were only 5 nm thick, the metals are reactive, and with the energy provided by heating, these layers easily decompose and the elements diffused to form grains 35 times larger than the initial layer. The magnetron sputtered film composed of Cu—Nb binary system also experienced rapid grain growth after heat treatment at 1000 °C for 1 min under vacuum, showing a grain size of 468 ± 185 nm [3]. The Ti—Cr—Zr system nanoscale multilayers with 10 nm layer thickness presented an average grain size of 7.6 nm after 5 min of heat treatment, Fig. 7a, and this size increased to 119.1 nm after 10 min, Fig. 9a. As anticipated, these findings demonstrate that the average grain size enlarged with longer heat treatment durations, as grain growth is a process governed by diffusion and thermally initiated mechanisms. For comparison, Ni—Zr magnetron sputtered coating exhibited an average grain size of 40 ± 12 nm after 1-min heat treatment at 1100 °C under vacuum conditions [3]. This grain size is larger than what was observed for Ti—Cr—Zr nanoscale system multilayer subjected to a longer heat treatment (5 min) at the same temperature.

Regarding the phases present before and after heat treatment, for the Ti—Cr—Zr nanoscale system multilayers with 5 nm individual layer thickness subjected to a 10-min heat treatment, the previously formed phases of Cr_4TiZr and $TiCr_2$, already present during deposition, was still present. Additionally, a new phase, $Ti_{0.3}Zr_{0.7}$, appear after 5 min of heat treatment: For the Ti—Cr—Zr nanoscale system multilayers with 10 nm individual layer thickness, after 10 min of heat treatment, the same phases formed during deposition were present, Cr_2Zr, Cr_4TiZr and $Ti_{0.3}Zr_{0.7}$, without the formation of any new phase. Notably, they also show that thinner nanolayers allow for faster diffusion, phase formation, and grain growth. This accelerated rate can be attributed to the greater interface volume, which in turn enhances reaction velocities. Conversely, in the Ti—Cr—Zr system nanoscale multilayers with 10 nm layer thickness, the precipitates exhibited a more pronounced growth, Fig. 9a, compared to the Ti—Cr—Zr system nanoscale multilayers with 5 nm individual layer thickness, Fig. 7a. This precipitate growth can act as mechanical and thermodynamic impediment to grain growth in the Ti—Cr—Zr system nanoscale multilayers with 10 nm layer thickness. A study revealed that high-temperature stabilization was achieved for Fe—10Cr—xZr and Fe—18Cr—xZr alloys through two potential mechanisms: Zener pinning of grain boundaries by $Zr(Fe_xCr_{1-x})$ intermetallic precipitates (a kinetic mechanism) or the segregation of Zr to grain boundaries (a thermodynamic mechanism). The results showed that the stabilized average grain size measured was 82 nm, whereas the Zener pinning model predicted a grain size of 168 nm. This additional stabilization was attributed to the thermodynamic mechanism [40]. Strategies in kinetic to hinder grain growth in nanocrystalline metals includes mechanisms as Zener pinning [57–59] or solute drag [60–62]. These mechanisms involve the constrained mobility of a secondary phase between crystallites, effectively reducing undesirable motion along grain boundary. Frequently, microstructures are stabilized through the combined effects of thermodynamic and kinetic approaches by introducing segregation dopants elements. This results in both grain boundary segregation and the emergence of second-phase particle that effectively pin grain boundaries [40,63,64]. Regarding the Ti—Cr—Zr system nanoscale multilayers, no conclusive evidence of Zr segregation to grain boundary was observed. Nevertheless, it is notable the presence of intermetallic formation and precipitates, thus it can impact grain growth by mechanically and thermodynamically impeding the movement of grain boundaries.

It can be observed that, in both cases, with layer thickness of 5 and 10 nm, the multilayer structure was entirely decomposed after heat treatment at 1100 °C for 10 min, Figs. 7a and 9a. This led to layer diffusion and the noticeable formation of grains. Additionally, STEM observations of both cases, multilayers with 5 and 10 nm layer thickness, after 1100 °C for 10 min, revealed the presence of twins, Figs. 7a and 9a. Previous research has established a strong correlation between the development and growth of annealing twins and grain growth. Specifically, the quantity and dimensions of these twins escalate with increasing time and temperature. This phenomenon is attributed to two distinct mechanisms responsible for twin nucleation and migration: variations in grain boundary mobility among faceted grain boundaries and the intersection of advancing grain boundaries with pre-existing twins [9]. Both of these mechanisms can be observed in the Ti-Cr-Zr system nanoscale multilayers.

5. Conclusions

The investigation into grain growth and phase formation within Ti-Cr-Zr system nanoscale multilayers fabricated by magnetron sputtering with 5 and 10 nm layer thickness, subjected to heat treatment at 1100 °C for 5 and 10 min It was done through X-ray Photoelectron Spectroscopy (XPS), X-Ray Diffraction (XRD) and Transmission Electron Microscopy (TEM) analysis. During the deposition process, evidence of diffusion was apparent as the multilayers manifest the formation of Cr_4TiZr, $TiCr_2$ and Cr_2Zr phases. The 10 nm individual layer thickness coating also presented the formation of $Ti_{0.3}Zr_{0.7}$ phase. During heat treatment, there was a reduction in the presence of pure metals, accompanied by an increase in the presence of the phases already formed during the deposition. After 5 min of heat treatment, grain sizes of 5.0 nm and 7.6 nm were observed for the Ti—Cr—Zr system nanoscale

multilayers with 5 and 10 nm layer thickness, respectively. Remarkably, a significant grain growth was noted after 10 min of heat treatment, resulting in average sizes of 173.7 nm and 119.1 nm for the Ti—Cr—Zr system nanoscale multilayers with 5 and 10 nm layer thickness, respectively. This discrepancy in growth rates between the 5 and 10 nm multilayers can be attributed to their differing interfacial volumes which subsequently affect the reaction velocity due to the varying thickness of the nano layers. Furthermore, the multilayers with 10 nm layer thickness exhibited larger precipitates compared to those with a 5 nm layer thickness, measuring 111.2 nm and 19.4 nm, respectively. These variations in precipitate growth notably influenced the restriction of grain growth in the Ti—Cr—Zr system nanoscale multilayers with 10 nm layer thickness. Despite grain growth, the coating continued to exhibit nanoscale dimensions as intended. The Ti—Cr—Zr system nanoscale multilayers with 5 nm individual layer thickness formed a new phase after heat treatment that was not present after deposition, the $Ti_{0.3}Zr_{0.7}$ phase On the other hand, the Ti—Cr—Zr system nanoscale multilayers with 10 nm individual layer thickness did not exhibit the formation of any new phase during heat treatment. Additionally, STEM analysis revealed the presence of twins in both the 5 and 10 nm layer thickness multilayers after 10 min of heat treatment. These twin defects are expected to form during the growth of nano grains. In conclusion, the desired nano grain stabilization of the Ti—Cr—Zr system nanoscale multilayers after heat treatment at 1100 °C for 10 min was achieved with the entirely decomposition of the multilayer structure and formation of grains smaller than 200 nm. As future consideration, it is crucial to conduct further observations to investigate the grain growth after extended heat treatment durations and ascertain the sustained preservation of the nanoscale grain sizes.

Funding

This research was supported by the Coordination of Superior Level Staff Improvement (CAPES) [grant number 88887.637029/2021-00] and the National Council for Scientific and Technological Development (CNPq) [grant number 166831/2022-0]. C.R.M.A., A.M.S.M. and H.C.P. acknowledge CNPq for their fellowship support.

CRediT authorship contribution statement

Júlia Nascimento Pereira: Data curation, Formal analysis, Investigation, Writing – original draft, Writing – review & editing. **Vincent Ott:** Data curation, Methodology. **Conrado Ramos Moreira Afonso:** Data curation, Formal analysis. **Artur Mariano de Sousa Malafaia:** Data curation, Resources, Writing – review & editing. **Michael Stüber:** Formal analysis, Investigation, Writing – review & editing. **Christian Greiner:** Conceptualization, Formal analysis, Resources, Writing – review & editing. **Haroldo Cavalcanti Pinto:** Conceptualization, Formal analysis, Funding acquisition, Methodology, Project administration, Resources, Supervision, Writing – review & editing.

Declaration of competing interest

The authors declare that they have no known competing financial interests or personal relationships that could have appeared to influence the work reported in this paper.

Data availability

Data will be made available on request.

Acknowledgments

The authors acknowledge the Brazilian agencies CAPES, and CNPq for providing scholarships. This research used facilities of the Brazilian Nanotechnology National Laboratory (LNNano), a division of the Brazilian Center for Research in Energy and Materials (CNPEM). CNPEM is a private, non-profit organization under the supervision of the Brazilian Ministry for Science, Technology, and Innovations (MCTI). Proposal number 20230706. The funding of the São Paulo Research Foundation (FAPESP) is also greatly acknowledged (Process 2019/14262-3).

References

[1] M. Dao, L. Lu, R.J. Asaro, J.T.M. De Hosson, E. Ma, Toward a quantitative understanding of mechanical behavior of nanocrystalline metals, Acta Mater. 55 (2007) 4041–4065, https://doi.org/10.1016/j.actamat.2007.01.038.
[2] H.A. Murdoch, C.A. Schuh, Estimation of grain boundary segregation enthalpy and its role in stable nanocrystalline alloy design, J. Mater. Res. 28 (2013) 2154–2163, https://doi.org/10.1557/jmr.2013.211.
[3] J.D. Schuler, T.J. Rupert, Materials selection rules for amorphous complexion formation in binary metallic alloys, Acta Mater. 140 (2017) 196–205, https://doi.org/10.1016/j.actamat.2017.08.042.
[4] V. Turlo, T.J. Rupert, Grain boundary complexions and the strength of nanocrystalline metals: dislocation emission and propagation, Acta Mater. 151 (2018) 100–111, https://doi.org/10.1016/j.actamat.2018.03.055.
[5] M.A. Meyers, A. Mishra, D.J. Benson, Mechanical properties of nanocrystalline materials, Prog. Mater. Sci. 51 (2006) 427–556, https://doi.org/10.1016/j.pmatsci.2005.08.003.
[6] X.Y. Zhang, M.H. Shi, C. Li, N.F. Liu, Y.M. Wei, The influence of grain size on the corrosion resistance of nanocrystalline zirconium metal, Mater. Sci. Eng. A 448 (2007) 259–263, https://doi.org/10.1016/j.msea.2006.10.029.
[7] N. Nita, R. Schaeublin, M. Victoria, Impact of irradiation on the microstructure of nanocrystalline materials, J. Nucl. Mater. 329–333 (2004) 953–957, https://doi.org/10.1016/j.jnucmat.2004.04.058.
[8] J. Weissmüller, Alloy thermodynamics in nanostructures, J. Mater. Res. 9 (1994) 4–7.
[9] S. Simoes, R. Calinas, M.T. Vieira, M.F. Vieira, P.J. Ferreira, In situ TEM study of grain growth in nanocrystalline copper thin films, Nanotechnology 21 (2010), https://doi.org/10.1088/0957-4484/21/14/145701.
[10] H. Natter, M. Schmelzer, M.S. Löffler, C.E. Krill, A. Fitch, R. Hempelmann, Grain-growth kinetics of Nanocrystalline Iron studied in situ by synchrotron real-time X-ray diffraction, J. Phys. Chem. B 104 (2000) 2467–2476, https://doi.org/10.1021/jp991622d.
[11] J.A. Haber, W.E. Buhro, Kinetic instability of nanocrystalline aluminum prepared by chemical synthesis; facile room-temperature grain growth, J. Am. Chem. Soc. 120 (1998) 10847–10855, https://doi.org/10.1021/ja981972y.
[12] V.Y. Gertsman, R. Birringer, On the room-temperature grain growth in nanocrystalline copper, Scr. Metall. Mater. 30 (1994) 577–581, https://doi.org/10.1016/0956-716X(94)90432-4.
[13] M. Ames, J. Markmann, R. Karos, A. Michels, A. Tschöpe, R. Birringer, Unraveling the nature of room temperature grain growth in nanocrystalline materials, Acta Mater. 56 (2008) 4255–4266, https://doi.org/10.1016/j.actamat.2008.04.051.
[14] K. Adam, D. Zöllner, D.P. Field, 3D microstructural evolution of primary recrystallization and grain growth in cold rolled single-phase aluminum alloys, Model. Simul. Mater. Sci. Eng. 26 (2018), https://doi.org/10.1088/1361-651X/aaa146.
[15] L. Li, T. Ungár, Y.D. Wang, G.J. Fan, Y.L. Yang, N. Jia, Y. Ren, G. Tichy, J. Lendvai, H. Choo, P.K. Liaw, Simultaneous reductions of dislocation and twin densities with grain growth during cold rolling in a nanocrystalline Ni-Fe alloy, Scr. Mater. 60 (2009) 317–320, https://doi.org/10.1016/j.scriptamat.2008.10.031.
[16] P.J. Kelly, R.D. Arnell, W. Ahmed, A. Afzal, Novel engineering coatings produced by closed-field unbalanced magnetron sputtering, Mater. Des. 17 (1996) 215–219, https://doi.org/10.1016/S0261-3069(97)00009-5.
[17] S. Korte-Kerzel, T. Hickel, L. Huber, D. Raabe, S. Sandlöbes-Haut, M. Todorova, J. Neugebauer, Defect phases–thermodynamics and impact on material properties, Int. Mater. Rev. 67 (2022) 89–117, https://doi.org/10.1080/09506608.2021.1930734.
[18] J. Weissmüller, Alloy effects in nanostructures, Nanostruct. Mater. 3 (1993) 261–272.
[19] M.N. Polyakov, T. Chookajorn, M. Mecklenburg, C.A. Schuh, A.M. Hodge, Sputtered Hf-Ti nanostructures: a segregation and high-temperature stability study, Acta Mater. 108 (2016) 8–16, https://doi.org/10.1016/j.actamat.2016.01.073.
[20] Y.Z. Chen, A. Herz, Y.J. Li, C. Borchers, P. Choi, D. Raabe, R. Kirchheim, Nanocrystalline Fe-C alloys produced by ball milling of iron and graphite, Acta Mater. 61 (2013) 3172–3185, https://doi.org/10.1016/j.actamat.2013.02.006.
[21] J.S. Riano, A.M. Hodge, Phase transformations in the W–Cr system at the nanoscale, Materialia 2 (2018) 190–195, https://doi.org/10.1016/j.mtla.2018.07.021.
[22] M. Bobeth, A. Ullrich, W. Pompe, Destratification mechanisms in coherent multilayers, J. Metastable Nanocrystal. Mater. 19 (2004) 153–178, https://doi.org/10.4028/www.scientific.net/jmnm.19.153.
[23] M. Kuzmina, M. Herbig, D. Ponge, S. Sandlöbes, D. Raabe, Linear complexions: confined chemical and structural states at dislocations, Science (80-.) 349 (2015) 1080–1083.
[24] C.D. Appleget, J.S. Riano, A.M. Hodge, An overview of nano multilayers as model systems for developing nanoscale microstructures, Materials (Basel) 14 (2021), https://doi.org/10.3390/xxxxx.

[25] M. Hecker, J. Thomas, D. Tietjen, S. Baunack, C.M. Schneider, A. Qiu, N. Cramer, R.E. Camley, Z. Celinski, Thermally induced modification of GMR in Co/Cu multilayers: correlation among structural, transport, and magnetic properties, J. Phys. D. Appl. Phys. 36 (2003) 564–572.

[26] D.E. Kimbrough, Y. Cohen, A.M. Winer, L. Creelman, A critical assessment of chromium in the environment, Crit. Rev. Environ. Sci. Technol. 29 (1999) 1–46.

[27] R.H. Nielsen, J.H. Schlewitz, H. Nielsen, Updated by staff, zirconium and zirconium compounds, Kirk-Othmer Encycl. Chem. Technol. (2013), https://doi.org/10.1002/0471238961.26091803.a01.pub3.

[28] R.R. Boyer, An overview on the use of titanium in the aerospace industry, Mater. Sci. Eng. A 213 (1996) 103–114, https://doi.org/10.1016/0921-5093(96)10233-1.

[29] R.L. Fleischer, R.J. Zabala, Mechanical properties of Ti-Cr-Nb alloys and prospects for high-temperature applications, Metall. Trans. A. 21 (1990) 2149–2154, https://doi.org/10.1007/BF02647875.

[30] J. Bodega, J.F. Fernández, F. Leardini, J.R. Ares, C. Sánchez, Synthesis of hexagonal C14/C36 and cubic C15 ZrCr2 laves phases and thermodynamic stability of their hydrides, J. Phys. Chem. Solids 72 (2011) 1334–1342, https://doi.org/10.1016/j.jpcs.2011.08.004.

[31] C.D. Rabadia, Y.J. Liu, L.Y. Chen, S.F. Jawed, L.Q. Wang, H. Sun, L.C. Zhang, Deformation and strength characteristics of laves phases in titanium alloys, Mater. Des. 179 (2019) 107891, https://doi.org/10.1016/j.matdes.2019.107891.

[32] C.D. Rabadia, Y.J. Liu, S.F. Jawed, L.Q. Wang, H. Sun, L.C. Zhang, Deformation and toughness behavior of β-type titanium alloys comprising C15-type laves phase, Mater. Today Sustain. 9 (2020) 100034, https://doi.org/10.1016/j.mtsust.2020.100034.

[33] F. Xu, X. Gao, H. Cui, Q. Song, R. Chen, Lightweight and high hardness (AlNbTiVCr)100-xNix high entropy alloys reinforced by laves phase, Vacuum 213 (2023) 112115, https://doi.org/10.1016/j.vacuum.2023.112115.

[34] A. Suzuki, N.D. Saddock, J.R. TerBush, B.R. Powell, J.W. Jones, T.M. Pollock, Precipitation strengthening of a Mg-Al-Ca-based AXJ530 die-cast alloy, Metall. Mater. Trans. A Phys. Metall. Mater. Sci. 39 A (2008) 696–702, https://doi.org/10.1007/s11661-007-9455-4.

[35] S.R. Ovshinsky, M.A. Fetcenko, J. Ross, A nickel metal hydride battery for electric vehicles, Stanford R. Ovshinsky Sci. Technol. Am. Genius 260 (2008) 214–219, https://doi.org/10.1142/9789812818416_0005.

[36] X. Chen, H. Yang, F. Pan, A special editor's issue on mg-based functional materials: design and development, J. Magnes. Alloy. 9 (2021) 1835–1836, https://doi.org/10.1016/j.jma.2021.11.001.

[37] C. Liu, Y. Gao, K. Chong, F. Guo, D. Wu, Y. Zou, Effect of Nb content on the microstructure and corrosion resistance of FeCoCrNiNbx high-entropy alloys in chloride ion environment, J. Alloys Compd. 935 (2023) 168013, https://doi.org/10.1016/j.jallcom.2022.168013.

[38] H. Ren, R.R. Chen, X.F. Gao, T. Liu, G. Qin, S.P. Wu, J.J. Guo, Development of wear-resistant dual-phase high-entropy alloys enhanced by C15 laves phase, Mater. Charact. 200 (2023) 1–10, https://doi.org/10.1016/j.matchar.2023.112879.

[39] M. Mizumaki, K. Yano, I. Umehara, F. Ishikawa, K. Sato, A. Koizumi, N. Sakai, T. Muro, Verification of Ni magnetic moment in GdNi2 laves phase by magnetic circular dichroism measurement, Phys. Rev. B - Condens. Matter Mater. Phys. 67 (2003) 2–5, https://doi.org/10.1103/PhysRevB.67.132404.

[40] M. Saber, H. Kotan, C.C. Koch, R.O. Scattergood, Thermal stability of nanocrystalline Fe-Cr alloys with Zr additions, Mater. Sci. Eng. A 556 (2012) 664–670, https://doi.org/10.1016/j.msea.2012.07.045.

[41] F.B. Cuff, N.J. Grant, C.F. Floe, Titanium-chromium phase diagram, J. Meteorol. (1952) 848–853.

[42] K.P. Gupta, The Cr-Ni-Zr (chromium-nickel-zirconium) system, J. Phase Equilib. Diffus. 31 (2010) 191–193, https://doi.org/10.1007/s11669-010-9666-z.

[43] Y. Arai, T. Marumo, R. Inoue, Use of zr–ti alloy melt infiltration for fabricating carbon-fiber-reinforced ultrahigh-temperature ceramic matrix composites, J. Compos. Sci. 5 (2021), https://doi.org/10.3390/jcs5070186.

[44] W. Gierlotka, C.Y. Lee, Thermodynamic description of hydrogen storage materials Cr-Ti-Zr and Fe-Ti-Zr, J. Mater. Res. 32 (2017) 1386–1396, https://doi.org/10.1557/jmr.2017.78.

[45] Y. Li, Z. Ru, Y. Cui, K. Luo, Phase stability and hardness of some ternary Ti-Zr based shape memory alloys, Int. J. Smart Nano Mater. 2 (2011) 272–282, https://doi.org/10.1080/19475411.2011.616952.

[46] V. Ott, C. Schäfer, S. Suarez, K. Woll, F. Mücklich, H.J. Seifert, S. Ulrich, C. Pauly, M. Stueber, Impact of microstructure of nanoscale magnetron sputtered Ru/Al multilayers on thermally induced phase formation, Coatings 13 (2023), https://doi.org/10.3390/coatings13010149.

[47] D.P. Adams, Reactive multilayers fabricated by vapor deposition: a critical review, Thin Solid Films 576 (2015) 98–128, https://doi.org/10.1016/j.tsf.2014.09.042.

[48] ISO 21608, Corros. Met. Alloy. - Test method isothermal-exposure Oxid. Test. under High-Temperature Corros. Cond. Met. Mater, 2012.

[49] Thermo-Calc Software - TCFe13. https://thermocalc.com/, 2023. (Accessed 1 December 2023).

[50] R. Simpson, R.G. White, J.F. Watts, M.A. Baker, XPS investigation of monatomic and cluster argon ion sputtering of tantalum pentoxide, Appl. Surf. Sci. 405 (2017) 79–87, https://doi.org/10.1016/j.apsusc.2017.02.006.

[51] I. Jacob, A. Stern, A. Moran, D. Shaltiel, D. Davidov, Hydrogen absorption in (ZrxTi1 -x) B2 (B ≡ Cr, Mn) and the phenomenological model for the absorption capacity in pseudo-binary laves-phase compounds, J. Less-Common Met. 73 (1980) 369–376, https://doi.org/10.1016/0022-5088(80)90331-8.

[52] N. Tamura, The concept of crystalline approximants for decagonal and icosahedral quasicrystals, Philos. Mag. A Phys. Condens. Matter Struct. Defects Mech. Prop. 76 (1997) 337–356, https://doi.org/10.1080/01418619708209979.

[53] G. Zheng Ma, P. Fei He, H. Dou Wang, H. Gang Tian, L. Zhou, Q. Song Yong, M. Liu, H. Chao Zhao, D. Yu He, Promoting bonding strength between internal Al-Si based gradient coating and aluminum alloy cylinder bore by forming homo-epitaxial growth interface, Mater. Des. 227 (2023), https://doi.org/10.1016/j.matdes.2023.111764.

[54] S. Bennett, A. Madan, Superhard superlattices, Phys. World 11 (1998) 45–48, https://doi.org/10.1098/rspa.1987.0086.

[55] R. Knepper, M.R. Snyder, G. Fritz, K. Fisher, O.M. Knio, T.P. Weihs, Effect of varying bilayer spacing distribution on reaction heat and velocity in reactive Al/Ni multilayers, J. Appl. Phys. 105 (2009), https://doi.org/10.1063/1.3087490.

[56] C. Pauly, K. Woll, I. Gallino, M. Stueber, H. Leiste, R. Busch, F. Mucklich, Ignition in ternary Ru/Al-based reactive multilayers - effects of chemistry and stacking sequence, J. Appl. Phys. 124 (2018).

[57] W.B. Li, K.E. Easterling, The influence of particle shape on zener drag, Acta Metall. Mater. 38 (1990) 1045–1052, https://doi.org/10.1016/0956-7151(90)90177-I.

[58] C. Schwarze, R. Darvishi Kamachali, I. Steinbach, Phase-field study of zener drag and pinning of cylindrical particles in polycrystalline materials, Acta Mater. 106 (2016) 59–65, https://doi.org/10.1016/j.actamat.2015.10.045.

[59] E. Nes, N. Ryum, O. Hunderi, On the Zener drag, Acta Metall. 33 (1985) 11–22.

[60] I. Toda-Caraballo, C. Capdevila, G. Pimentel, C.G. De Andrés, Drag effects on grain growth dynamics, Comput. Mater. Sci. 68 (2013) 95–106, https://doi.org/10.1016/j.commatsci.2012.10.012.

[61] J.W. Cahn, The impurity-drag effect in grain boundary motion, Acta Metall. 10 (1962) 789–798, https://doi.org/10.1016/0001-6160(62)90092-5.

[62] M.I. Mendelev, D.J. Srolovitz, Impurity effects on grain boundary migration, Model. Simul. Mater. Sci. Eng. 10 (2002), https://doi.org/10.1088/0965-0393/10/6/201.

[63] C.C. Koch, R.O. Scattergood, M. Saber, H. Kotan, High temperature stabilization of nanocrystalline grain size: thermodynamic versus kinetic strategies, J. Mater. Res. 28 (2013) 1785–1791, https://doi.org/10.1557/jmr.2012.429.

[64] D. Amram, C.A. Schuh, Interplay between thermodynamic and kinetic stabilization mechanisms in nanocrystalline Fe-Mg alloys, Acta Mater. 144 (2018) 447–458, https://doi.org/10.1016/j.actamat.2017.11.014.